A Wideband Fabry-Pérot Antenna With Enhanced Gain in the High-Frequency Operating Band by Adopting a Truncated Field Correcting Structure

Zhiming Liu, Jens Bornemann, *Life Fellow, IEEE*, Deisy Formiga Mamedes, *Graduate Student Member, IEEE*, Shaobin Liu, *Member, IEEE*, Xiangkun Kong, *Member, IEEE*, and Xing Zhao

***Abstract*— A novel method to enhance the high-frequency gain of a wideband Fabry–Pérot (FP) antenna by using a truncated field correcting structure (TFCS) is proposed. The TFCS is formed by laminated dual-layer dielectric substrates and acts as the high-frequency operating band phase and amplitude correcting structure of the FP antenna for the radiated field. This method not only has a small effect on the operating bandwidth of the antenna, but also has a positive effect on improving the gain over the low-frequency operating band. The simulation and experimental results verify that the TFCS can effectively enhance the gain within the high-frequency operating band, and expand the 3 dB gain bandwidth of the FP antenna. The measured results show that the proposed antenna has a 10 dB return loss bandwidth of 8.49–12.34 GHz (37.0%), a 3 dB gain bandwidth of 8.48–11.82 GHz (32.9%), and a maximum gain of 17.73 dBi. The 3 dB gain bandwidth of the FP antenna is extended from 28.8% to 32.9% after loading with the TFCS, and the maximum gain enhancement within the high-frequency operating band is increased by 3.48 dB at 11.58 GHz.**

***Index Terms*— Bandwidth enhancement, Fabry–Pérot (FP) antenna, high gain, wideband.**

I. Introduction

FABRY–PÉROT (FP) antennas are also called partially reflective surface (PRS) antennas, 2-D leaky-wave antennas, electromagnetic bandgap (EBG) resonator antennas, resonant cavity antennas, and FP resonator antennas [1]–[7]. They are basically composed of a PRS and a primary antenna where the FP resonant cavity is formed by the ground of the primary antenna and the PRS. In early stages, the FP resonant cavity had high Q-value characteristics, which enabled FP antennas to exhibit high gain and narrowband properties. With the advance of FP antenna research, they can achieve properties such as wide bandwidth [8], [9], low profile [10], [11], circular polarization [12], [13], multiband operation [14], reconfigurability [15]–[17], and low RCS [18]–[20], which provide them with a broad application prospect in the field of wireless communication.

For wideband FP antennas, various methods for expanding the 3 dB gain bandwidth have been proposed [21]–[30]. Generally, PRSs are used which adopt printed or all-dielectric structures. The printed PRS structures of wideband FP antennas can be divided into two categories: nonuniformly printed PRSs [21], [22] and uniformly printed PRSs [8], [23]–[25]. More recently, all-dielectric PRS structures have been introduced to expand the bandwidth of FP antennas, including single-layer all-dielectric transverse permittivity gradient (TPG) PRS structures [26], [27], a multilayer all-dielectric PRS with small footprint [28], multilayer all-dielectric TPG PRS structures [29], [30], a multilayer truncated all-dielectric PRS structure [31], and a near-field correction all-dielectric PRS structure [32]. Note that near-field manipulation can be applied to improve various properties of antennas, such as the bandwidth [32], directivity [33], and beam steering [34]. It can also be observed that most of all-dielectric PRSs provide superior gain enhancement and bandwidth expansion capabilities compared with printed PRS structures.

Although many efforts focused on extending the 3 dB gain bandwidth of FP antennas, it was found that wideband FP antennas, which employ a uniform printed PRS with positive reflection phase gradient, exhibit a sharp gain drop in the high-frequency operating band. This is due to the fact that the reflection phase of PRSs drops significantly toward high frequencies [35]–[39]. There are several ways to improve the gain and the gain bandwidth of FP antennas. In [31], a multilayer truncated PRS is effectively used to excite the resonance of the FP cavity at both low and high frequencies,

Manuscript received October 1, 2020; revised May 20, 2021; accepted May 22, 2021. Date of publication June 25, 2021; date of current version December 16, 2021. This work was supported in part by the Natural Sciences and Engineering Research Council (NSERC) of Canada, in part by Chinese Natural Science Foundation under Grant 62071221 and Grant 62071227, in part by the Fundamental Research Funds for the Central Universities under Grant kfjj20200403, and in part by Jiangsu Planned Projects for Postdoctoral Research Funds under Grant 2019K018A. *(Corresponding author: Jens Bornemann.)*

Zhiming Liu was with the Department of Electrical and Computer Engineering, University of Victoria, Victoria, BC V8W 2Y2, Canada. He is now with the School of Information Engineering, Nanchang University, Nanchang 330031, China (e-mail: lzmedu@foxmail.com).

Jens Bornemann and Deisy Formiga Mamedes are with the Department of Electrical and Computer Engineering, University of Victoria, Victoria, BC V8W 2Y2, Canada (e-mail: j.bornemann@ieee.org).

Shaobin Liu, Xiangkun Kong, and Xing Zhao are with the College of Electronic and Information Engineering, Nanjing University of Aeronautics and Astronautics, Nanjing 210016, China.

Color versions of one or more figures in this article are available at https://doi.org/10.1109/TAP.2021.3090841.

Digital Object Identifier 10.1109/TAP.2021.3090841

which provides the excitation of the FP resonance in a wider band. However, its disadvantage is that the reflection amplitude of the truncated PRS is small at the low and high resonant frequencies, which affects the ability of the FP resonance to enhance the gain. In [37], a hybrid reflection method is presented to improve the 3 dB gain bandwidth of an FP antenna. Although two adjacent positive reflection phase gradient bands are obtained to optimally excite the low- and high-frequency FP resonances through two FSS units on the PRS, the gain deterioration within the high-frequency operating band is still unresolved. In [40], a quasi-curve reflector is proposed to improve the operating bandwidth and gain of an FP antenna by exciting a multimode response. This design is not only complicated, but the gain in the high-frequency operating band is still significantly reduced. In [41], a shaped ground plane is employed to extend the 3 dB gain bandwidth. This increases the difficulty of the ground design, and the inclination angle of the shaped ground is sensitive to the return loss bandwidth and the 3 dB gain bandwidth. Also, the use of optimization algorithms in FP antenna design is an important means to improve gain and gain bandwidth [32], [42]. In summary, the deterioration of the high-frequency gain of wideband FP antennas is a common problem, and seeking ways to improve it is of great value for expanding the gain bandwidth of FP antennas.

This article focuses on a novel method to enhance the gain of wideband FP antennas in the high-frequency operating band. A truncated field correcting structure (TFCS) is located directly above the FP antenna to manipulate the phase and amplitude distributions of the aperture field within the high-frequency operating band, thereby enhancing the gain of the FP antenna toward higher frequencies and expanding the 3 dB gain bandwidth. Moreover, the TFCS has little effect on the 10 dB return loss bandwidth and has a positive effect on the gain in the low-frequency operating band. The measured results show that the proposed antenna has a 10 dB return loss bandwidth of 8.49–12.34 GHz (37.0%), the 3 dB gain bandwidth is increased from 28.8% to 32.9%, the maximum gain is increased from 17.03 to 17.56 dBi, and the maximum gain enhancement at the high-frequency operating band is 3.48 dB.

II. Antenna Configuration

The geometric configuration of a primary antenna, consisting of a slot antenna and a parasitic patch, is depicted in Fig. 1(a). Note that other types of antennas that meet the requirements, such as a probe-fed microstrip antenna, dipole antenna, or waveguide-fed slot antenna, can also be used as the primary antenna. The parasitic patch is placed a distance h_{air} above the slot antenna, and its length and width are both $W = 80$ mm. The metal structure of the slot antenna and the parasitic patch are etched on Rogers RT5880 ($\varepsilon_{\text{r1}} = 2.2$, $\tan\delta = 0.0009$) substrate with a thickness of h_1, and the square patch size of the parasitic patch is w_{p}. Fig. 1(b) shows the overall structure of a FP antenna. It consists of the primary antenna shown in Fig. 1(a) and a PRS; the thickness of the cavity is h_{c}. The PRS consists of 9 × 9 FSS units etched on

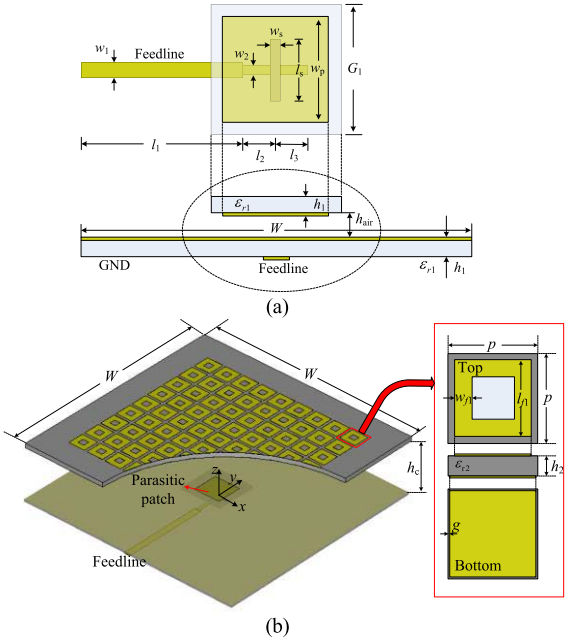

Fig. 1. Geometric configurations of antenna. (a) Primary antenna. (b) FP antenna.

TABLE I
Parameter of Slot-Coupled Patch Antenna

Parameters	h_1	h_{air}	l_1	l_2	l_3	l_{s}
Value (mm)	0.787	2.4	31.5	8.5	3	8.6
Parameters	h_2	w_{p}	w_{d}	w_1	w_2	w_{s}
Value (mm)	1.524	9.3	15	2.3	1.2	1
Parameters	p	h_c	G_1	l_{fl}	w_{fl}	g
Value (mm)	7	18	15	6	1.9	0.1

Rogers RT6002 ($\varepsilon_{\text{r2}} = 2.94$, $\tan\delta = 0.0012$) substrate with a thickness of h_2. The FSS unit consists of a patch and a metal square ring. Mutual coupling between the patch and the metal square ring is required to produce a proper positive reflection phase gradient and reflection amplitude. Note that the PRS can be replaced by other printed structures with similar properties. CST is employed for numerical simulation, periodic boundaries are applied to the simulation of unit structures, and open boundaries are used to simulate the FP antennas. Fig. 2(a) shows the reflection coefficient of the FSS unit, which displays a positive reflection phase gradient band between 9.54 and 10.86 GHz, and the reflection amplitude is greater than 0.59. The structural parameters are shown in Table I.

Fig. 2(b) shows the simulated results of the primary antenna and the FP antenna. It is observed that the primary antenna has a 10 dB return loss bandwidth of 9.04–11.57 GHz, and a maximum gain of 9.13 dBi at 11.2 GHz. The FP antenna has a 10 dB return loss bandwidth of 8.49–12.23 GHz, a 3 dB gain bandwidth of 8.46–10.99 GHz, and a maximum gain of 17.04 dBi at 9.3 GHz. The simulated results demonstrate the FP cavity's ability to enhance the gain of the antenna and expand its 10 dB return loss bandwidth. However, the gain of the FP antenna drops sharply between 11 and 12.23 GHz

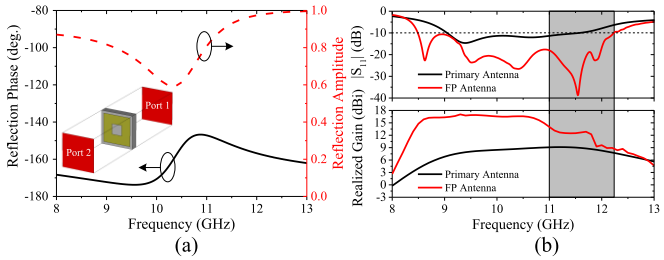

Fig. 2. (a) Simulated reflection coefficient of FSS. (b) Simulated $|S_{11}|$ and realized gain of FP antenna.

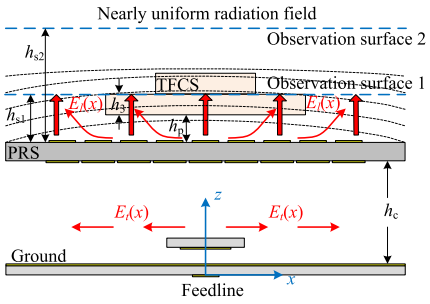

Fig. 3. Leaky-wave model of the FP antenna.

due to the fact that the reflection phases of the PRS cannot be fully adjusted to meet the resonant conditions of the FP cavity in this high-frequency operating band. To resolve this issue, Section III introduces a TFCS to improve the high-frequency gain of the FP antenna.

III. TFCS

The working mechanism of FP antennas can be explained by leaky-wave theory, as shown in Fig. 3. The FP cavity is formed between the ground and the PRS. As the primary antenna is excited, the electromagnetic wave $E_t(x)$ propagates in the cavity from the central area to the edge along the x-axis, which can be expressed as [43]

$$E_t(x) = E_0 e^{-\mathrm{sgn}(x)\int_0^x \gamma(\zeta)d\zeta} \tag{1}$$

where E_0 represents the source, γ represents the propagation constant, and $\mathrm{sgn}(x)$ is the signum function at position x inside the cavity. Since the PRS possesses characteristics of partial reflection, a part of the electromagnetic wave propagates in the cavity, passes through the PRS, and leaks out of the cavity to generate the leaky wave $E_l(x)$. The expressions of the phase and amplitude of the leaky wave are

$$\varphi_l(x) = \theta_{PRS}(x) - \mathrm{sgn}(x)\int_0^x \beta(\zeta)d\zeta \tag{2}$$

$$|E_l(x)| = C\sqrt{\alpha(x)}E_0 e^{-\mathrm{sgn}(x)\int_0^x \alpha(\zeta)d\zeta} \tag{3}$$

where C represents a constant variable, and α and β represent the attenuation and phase constants, respectively. Note that the phase of the leaky wave is related to the phase constant, while the amplitude is related to the attenuation constant. A nonuniform phase distribution of the radiated field leads to the divergence of radiant energy, and a nonuniform amplitude

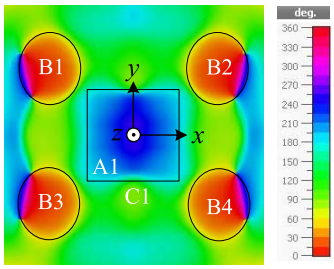

Fig. 4. Simulated phase distribution of the FP antenna on observation surface 1 at 11.5 GHz.

distribution causes a relatively low aperture efficiency of the FP antenna. However, the phase and attenuation constants are strongly correlated in a way that they interfere with each other, which poses a major challenge for the design of wideband FP antennas with high gain, especially in the high-frequency operating band.

A TFCS is proposed to correct the radiated field properties of the FP antenna at high frequencies. From Section II, it can be seen that the gain of the FP antenna drops sharply within the operating band between 11 and 12.23 GHz; therefore, 11.5 GHz is selected as a frequency of observation. Fig. 4 shows the simulated phase distribution of the FP antenna on observation surface 1 with a height of $h_{s1} = 6.024$ mm above the PRS. It can be observed that there is a single square phase area (A1) in the center of observation surface 1, and four phase areas (B1–B4) are generated on the four corners due to the edge effect of the PRS. Therefore, the key research direction of high-frequency gain enhancement is to optimize the high-frequency radiation phase and amplitude distributions so that the high-frequency radiated waves tend to be plane waves. From Fig. 4, the phase difference between the average phase value of area A1 and the surrounding area C1 is approximately 50°. In this case, the phase value of area A1 should be reduced by about 50° through a phase correction structure.

Dielectric loading is one of the important measures to modulate the phase distribution in the primary direction of radiation. Therefore, a single-layer square dielectric substrate is adopted, first, to compensate for the phases of area A1 on observation surface 1. Considering prototype fabrication and the phase compensation properties of the dielectric substrate, Rogers TMM 4 ($\varepsilon_{r3} = 4.5$, $\tan\delta = 0.002$) with a thickness of $h_3 = 1.524$ mm is selected as the field correcting structure (FCS). Fig. 5(a) depicts the simulated phase compensation of the FCS and shows that the phase compensation value of the FCS at 11.5 GHz is $-52°$, which meets the phase compensation requirement. The size and height of the FCS are the main factors that affect the performance of the FP antenna. They not only have to ensure the improvement of high-frequency radiation characteristics, but also should affect the low-frequency characteristics of the antenna as little as possible. After optimizing the design, the size of the FCS is $P_1 = 40$ mm, and it is placed $h_p = 4.5$ mm away from the PRS. Fig. 5(b) shows the phase distributions of the FP antenna with FCS on observation surface 1 at 11.5 GHz. It can be seen

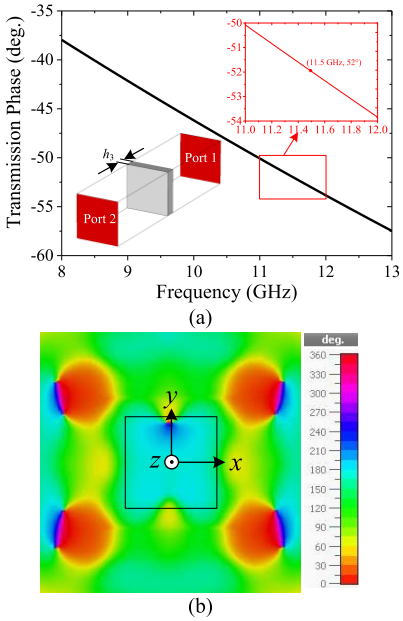

Fig. 5. (a) Simulated phase compensation curve of the FCS. (b) Simulated phase distributions of the FP antenna with FCS on the observation surface 1 at 11.5 GHz.

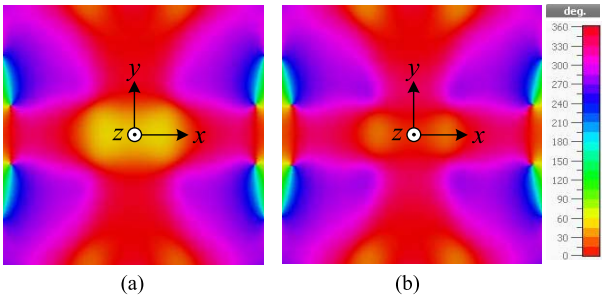

Fig. 6. Phase distributions of FP antenna on observation surface 2 at 11.5 GHz. (a) Loaded with FCS. (b) Loaded with TFCS.

that the phase distribution of the FP antenna in the central square area has been greatly improved.

Secondly, affected by the phase areas at the four corners, the non-uniformity of the phase distribution of the FP antenna will be increased when the electromagnetic waves propagate to a higher height in the propagation direction. In order to further optimize the phase distributions of the FP antenna at a higher distance, an observation surface 2 is set at a height of $h_{s2} = 16.7$ mm above the PRS. Fig. 6(a) shows the phase distribution of the FP antenna with FCS on observation surface 2 at 11.5 GHz. We note that the phase distribution of observation surface 2 in the central yellow area can be optimized and that the phase difference between the central yellow area and the surrounding red area is about 50°. Therefore, a small square dielectric substrate with the same dielectric as the FCS is laminated on top of the above FCS to form a TFCS. The optimized size of the small square dielectric substrate is $P_2 = 20$ mm. According to the numerical simulation, the size of the TFCS will affect the gain bandwidth of the antenna. When P_1 and P_2 increase, the gain at 11 GHz decreases,

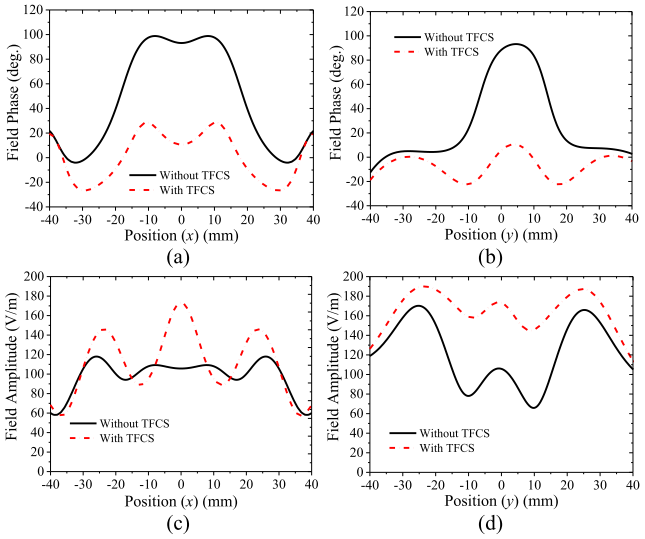

Fig. 7. Electric-field phase distributions versus (a) x and (b) y; and amplitude distributions versus (c) x and (d) y for the FP antenna with/without TFCS on observation surface 2 at 11.5 GHz.

which affects the 3 dB gain bandwidth of the proposed antenna. Meanwhile, the gain enhancement at high frequencies increases with the increase of P_1 and P_2. Fig. 6(b) shows the phase distribution of the FP antenna with TFCS on observation surface 2 at 11.5 GHz. Obviously, the phase distributions of the FP antenna with TFCS in the central area have been improved.

Moreover, the uniformities of the phase distribution of the electric field E_y along the x-axis ($y = 0$) and y-axis ($x = 0$) are increased, as shown in Fig. 7(a) and (b). The FP antenna with TFCS can obtain a relatively uniform electric-field phase distribution between -20 and 20 mm at 11.5 GHz compared with the original FP antenna on observation surface 2. Fig. 7(c) and (d) show the amplitude distributions of the electric field E_y along the x-axis ($y = 0$) and y-axis ($x = 0$) at 11.5 GHz. They show that the uniformity of the amplitude distribution along the x-axis is weakened, while the uniformity of the amplitude distribution along the y-axis is enhanced. This is due to the fact that in the x-direction, the TFCS does not completely cover the central phase singular area to prevent the gain sagging around 11 GHz, so as to ensure that the antenna has a relatively wide 3 dB gain bandwidth. Also, the field amplitude of the FP antenna with TFCS is larger than that of the original FP antenna. This is due to the fact that the TFCS moves the positive gradient reflection phase band of the PRS toward higher frequencies, which enhances the FP resonance of the cavity. This proves that the TFCS can not only modulate the phase distribution of the radiated field, but also has the ability to manipulate the uniformity of the electric-field amplitude distribution.

Fig. 8 shows the phase distributions of the three antennas in the xz plane at 11.5 GHz. It can be seen that the electromagnetic waves in the radiation direction of the FP antenna with TFCS tend to be plane waves, which is the essence of the high-frequency gain improvement of the FP antenna with TFCS. Moreover, this TFCS has the capability to manipulate radiated waves at frequencies around 11.5 GHz, but its ability

TABLE II
COMPARISON BETWEEN THE DESIGNED ANTENNA AND EXISTING WORKS

Ref.	Realization method	10-dB return loss bandwidth (GHz)	3-dB gain bandwidth (GHz)	Maximum Gain (dBi)	GBP	Area (λ_0^3)
[31]	CAMS	9.42-11.35 (18.6%)	16.58%	About 11.8	251	2.20×2.20×0.57
[33]	HPRS	8.64-12.07 (33.1%)	8.6-11.1 (25.4%)	17.08	1297	2.81×2.81×0.69
[34]	Embedded CPCM	8.48-12.21 (36.1%)	8.9-11.5 (25.5%)	17.2	1338	2.76×2.76×0.73
[36]	Quasi-curve reflector	24%	10%	16.3	427	10.0×5.80×1.40
[37]	Shaped Ground	19.7%	23%	16	916	2.75×2.75×0.56
This work	TFCS	8.49-12.34 (37.0%)	8.48-11.82 (32.9%)	17.73	1951	2.77×2.77×0.96

Note: GBP=BW×$10^{G/10}$, where GBP denotes the gain-bandwidth product, BW denotes the 3-dB gain bandwidth, G denotes the maximum gain. λ_0 denotes the wavelength at the center frequency of the effective bandwidth in free space. CAMS, HPRS, CPCM are abbreviations of chessboard arranged metamaterial superstrate, hybrid partially reflecting surface, and chessboard polarization conversion metasurface, respectively.

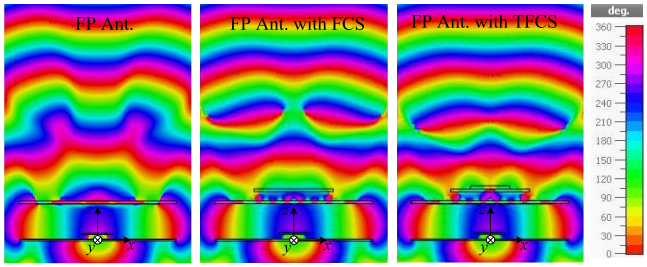

Fig. 8. Phase distributions of three antennas in the *xz* plane at 11.5 GHz.

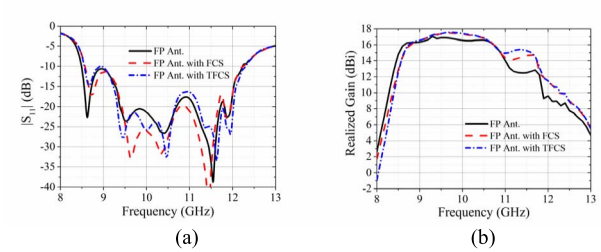

Fig. 9. Simulated results of the three antennas. (a) $|S_{11}|$ and (b) realized gain.

is weakening as the operating frequency moves away from 11.5 GHz.

Fig. 9 shows the simulated results of $|S_{11}|$ and realized gain of the FP antennas. It is observed that the operating band of the FP antenna is almost unchanged after loading with the TFCS and that the gain in the high-frequency operating band is enhanced. The FP antenna with TFCS has a 10 dB return loss bandwidth of 8.56–12.31 GHz (35.9%), a 3 dB gain bandwidth of 8.60–11.71 GHz (30.6%), and a maximum gain of 17.56 dBi at 9.7 GHz. Compared with the original FP antenna, the maximum gain enhancement of the FP antenna with FCS in the high-frequency operating band is 2.15 dB (11.5 GHz), while the maximum gain enhancement of the FP antenna with TFCS is 2.91 dB. Moreover, the gain around 10 GHz has been enhanced, which is due to the increase in the reflection amplitude of the PRS in this band after loading with the TFCS.

IV. MEASUREMENTS

The designed high-gain wideband FP antenna has been fabricated and measured. The prototype consists of a wideband slot-coupled antenna, a PRS, and a TFCS. The primary antenna structure is etched on Rogers RT5880 ($\varepsilon_{r1} = 2.2$, $\tan\delta = 0.0009$) substrate with a thickness of 0.787 mm, and the PRS is etched on Rogers RT6002 ($\varepsilon_{r2} = 2.94$, $\tan\delta = 0.0012$) substrate with a thickness of 1.524 mm; $W = 80$ mm in length and width, and the TFCS structure is composed of two layers of Rogers TMM 4 ($\varepsilon_{r3} = 4.5$, $\tan\delta = 0.002$) substrates with different sizes. The overall size of the antenna is 80 mm × 80 mm × 27.859 mm. The measurement of the proposed antenna is completed in a microwave anechoic chamber, and the experimental environment is shown in Fig. 10.

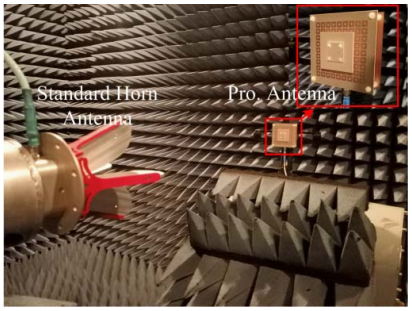

Fig. 10. Measurement setup of the proposed antenna.

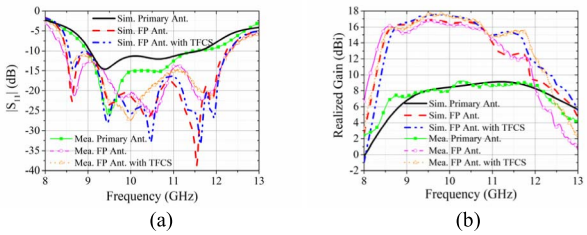

Fig. 11. Measured results of the proposed antenna. (a) $|S_{11}|$. (b) Realized gain.

Fig. 11 shows the measured results of $|S_{11}|$ and realized gain of the three different antennas. It is observed that the primary antenna has a 10 dB return loss bandwidth of 8.98–11.45 GHz (24.2%) and a maximum gain of 9.05 dBi at 11.77 GHz; the original FP antenna has a 10 dB return loss bandwidth of 8.41–12.31 GHz (37.6%), a 3 dB gain bandwidth of 8.34–11.15 GHz (28.8%), and a maximum gain of 16.82 dBi at 9.51 GHz. The proposed antenna with TFCS has a 10 dB return loss bandwidth of 8.49–12.34 GHz (37.0%), a 3 dB gain bandwidth of 8.48–11.82 GHz (32.9%), and a maximum gain of 17.73 dBi at 9.53 GHz, which are consistent with the simulated results. Also, compared with the original

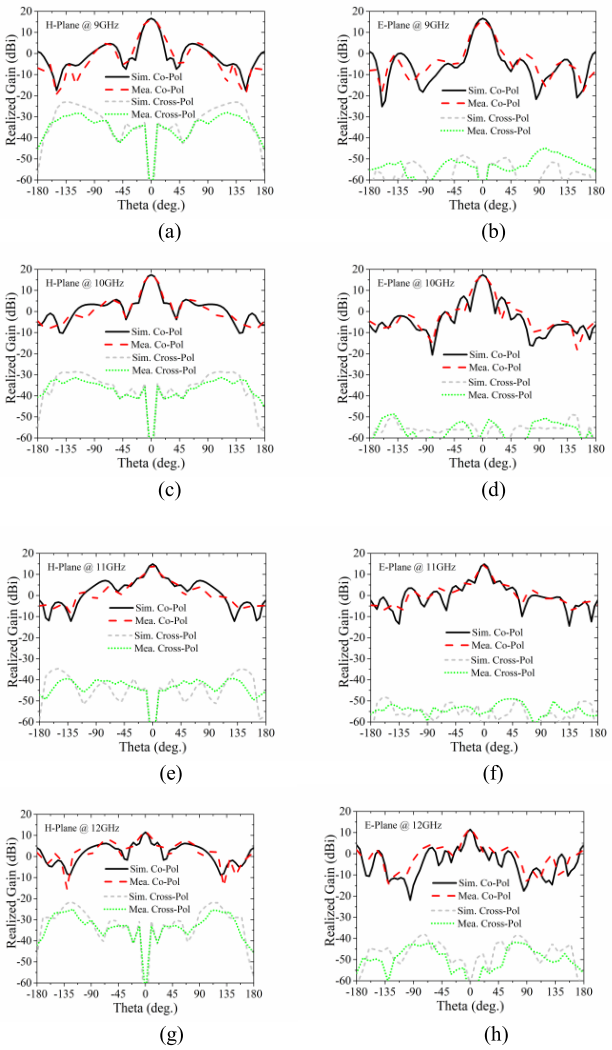

Fig. 12. Co-pol and cross-pol radiation patterns of the proposed antenna. (a) H-plane and (b) E-plane at 9 GHz. (c) H-plane and (d) E-plane at 10 GHz. (e) H-plane and (f) E-plane at 11 GHz. (g) H-plane and (h) E-plane at 12 GHz.

FP antenna, the maximum gain enhancement of the proposed antenna within the high-frequency operating band is 3.48 dB at 11.58 GHz, while the relatively 3 dB gain bandwidth is improved from 28.8% to 32.9%.

Fig. 12 displays the simulated and measured radiation patterns in E- and H-planes at 9, 10, 11, and 12 GHz which prove that the proposed antenna has good radiation characteristics. Moreover, it is observed that the simulated and measured cross-polarization levels are lower than -20 dB in both planes. Table II shows the performance comparison between the proposed antenna and comparable existing works. It is found that the proposed FP antenna has excellent 10 dB return loss bandwidth and 3 dB gain bandwidth. The essential reason for the 3 dB gain bandwidth expansion of the FP antenna is that the TFCS effectively improves the gain toward the high-frequency operating band.

V. Conclusion

A TFCS is employed to adjust the radiated field of a wideband FP antenna within the high-frequency operating band. The TFCS adopts a stacked structure of dual-layer dielectric substrates with different sizes, which can effectively enhance the gain by correcting the phase and amplitude distributions of radiated waves in the high-frequency operating band. Also, the TFCS not only has almost no effect on the impedance matching bandwidth but also enhances the gain of the low-frequency operating band. Experiments show that the proposed FP antenna has a 10 dB return loss bandwidth of 8.49–12.34 GHz (37.0%), a 3 dB gain bandwidth of 8.48–11.82 GHz (32.9%), and a maximum gain of 17.73 dBi at 9.53 GHz. Moreover, after loading with the TFCS, the maximum gain enhancement of the FP antenna within the high-frequency operating band reaches 3.48 dB. It demonstrates that this method is of great significance for expanding the 3 dB gain bandwidth and enhancing high-frequency operating characteristics of FP antennas.

References

[1] G. V. Trentini, "Partially reflecting sheet arrays," *IRE Trans. Antennas Propag.*, vol. 4, no. 4, pp. 666–671, Oct. 1956.
[2] D. R. Jackson and A. A. Oliner, "A leaky-wave analysis of the high-gain printed antenna configuration," *IEEE Trans. Antennas Propag.*, vol. AP-36, no. 7, pp. 905–910, Jul. 1988.
[3] C. Cheype, C. Serier, M. Thevenot, T. Monediere, A. Reineix, and B. Jecko, "An electromagnetic band gap resonator antenna," *IEEE Trans. Antennas Propag.*, vol. 50, no. 9, pp. 1285–1290, Sep. 2002.
[4] T. Zhao, D. R. Jackson, J. T. Williams, and A. A. Oliner, "General formulas for 2-D leaky-wave antennas," *IEEE Trans. Antennas Propag.*, vol. 53, no. 11, pp. 3525–3533, Nov. 2005.
[5] A. R. Weily, T. S. Bird, and Y. J. Guo, "A reconfigurable high-gain partially reflecting surface antenna," *IEEE Trans. Antennas Propag.*, vol. 56, no. 11, pp. 3382–3390, Nov. 2008.
[6] A. Foroozesh and L. Shafai, "Investigation into the effects of the reflection phase characteristics of highly-reflective superstrates on resonant cavity antennas," *IEEE Trans. Antennas Propag.*, vol. 58, no. 10, pp. 3392–3396, Oct. 2010.
[7] K. Lu and K. W. Leung, "Differential Fabry–Pérot resonator antennas," *IEEE Trans. Antennas Propag.*, vol. 61, no. 9, pp. 4438–4446, Sep. 2013.
[8] N. Wang, Q. Liu, C. Wu, L. Talbi, Q. Zeng, and J. Xu, "Wideband Fabry–Pérot resonator antenna with two complementary FSS layers," *IEEE Trans. Antennas Propag.*, vol. 62, no. 5, pp. 2463–2471, May 2014.
[9] N. Wang, J. Li, G. Wei, L. Talbi, Q. Zeng, and J. Xu, "Wideband Fabry–Pérot resonator antenna with two layers of dielectric superstrates," *IEEE Antennas Wireless Propag. Lett.*, vol. 14, pp. 229–232, Sep. 2015.
[10] Y. Sun, Z. N. Chen, Y. Zhang, H. Chen, and T. S. P. See, "Subwavelength substrate-integrated Fabry–Pérot cavity antennas using artificial magnetic conductor," *IEEE Trans. Antennas Propag.*, vol. 60, no. 1, pp. 30–35, Jan. 2012.
[11] Z. Liu, S. Liu, B. Bian, X. Kong, and H. Zhang, "Metasurface-based low-profile high-gain substrate-integrated Fabry–Pérot cavity antenna," *Int. J. RF Microw. Comput. Aided Eng.*, vol. 29, no. 4, Oct. 2018, Art. no. e21583.
[12] F. Qin *et al.*, "Wideband circularly polarized Fabry–Pérot antenna [Antenna applications corner]," *IEEE Antennas Propag. Mag.*, vol. 57, no. 5, pp. 127–135, Oct. 2015.
[13] Z. G. Liu, Z. X. Cao, and L. N. Wu, "Compact low-profile circularly polarized Fabry–Pérot resonator antenna fed by linearly polarized microstrip patch," *IEEE Antennas Wireless Propag. Lett.*, vol. 15, no. 7, pp. 524–527, Jul. 2016.
[14] B. A. Zeb and K. P. Esselle, "Design and measurements of a tri-band one-dimensional electromagnetic bandgap resonator antenna," *IET Microw., Antennas Propag.*, vol. 10, no. 2, pp. 168–172, Jan. 2016.
[15] R. Guzmán-Quirós, A. R. Weily, J. L. Gómez-Tornero, and Y. J. Guo, "A Fabry–Pérot antenna with two-dimensional electronic beam scanning," *IEEE Trans. Antennas Propag.*, vol. 64, no. 4, pp. 1536–1541, Apr. 2016.
[16] C. Huang, W. Pan, X. Ma, and X. Luo, "A frequency reconfigurable directive antenna with wideband low-RCS property," *IEEE Trans. Antennas Propag.*, vol. 64, no. 3, pp. 1173–1178, Mar. 2016.

[17] R. Lian, Z. Tang, and Y. Yin, "Design of a broadband polarization-reconfigurable Fabry–Pérot resonator antenna," *IEEE Antennas Wireless Propag. Lett.*, vol. 17, no. 1, pp. 122–125, Jan. 2018.

[18] W. Pan, C. Huang, P. Chen, X. Ma, C. Hu, and X. Luo, "A low-RCS and high-gain partially reflecting surface antenna," *IEEE Trans. Antennas Propag.*, vol. 62, no. 2, pp. 945–949, Feb. 2014.

[19] Y. Jia, Y. Liu, W. Zhang, J. Wang, S. Gong, and G. Liao, "High-gain Fabry–Pérot antennas with wideband low monostatic RCS using phase gradient metasurface," *IEEE Access*, vol. 7, pp. 4816–4824, Dec. 2019.

[20] J. Mu, H. Wang, H. Wang, and Y. Huang, "Low-RCS and gain enhancement design of a novel partially reflecting and absorbing surface antenna," *IEEE Antennas Wireless Propag. Lett.*, vol. 16, pp. 1903–1906, Mar. 2017.

[21] Z. G. Liu, R. Qiang, and Z. X. Cao, "A novel broadband Fabry–Pérot resonator antenna with gradient index metamaterial superstrate," in *Proc. IEEE Antennas Propag. Soc. Int. Symp.*, Jul. 2010, pp. 1–4.

[22] Z. Liu, W. Zhang, D. Fu, Y. Gu, and Z. Ge, "Broadband Fabry–Pérot resonator printed antennas using FSS superstrate with dissimilar size," *Microw. Opt. Technol. Lett.*, vol. 50, no. 6, pp. 1623–1627, 2008.

[23] Y. Ge, K. P. Esselle, and T. S. Bird, "The use of simple thin partially reflective surfaces with positive reflection phase gradients to design wideband, low-profile EBG resonator antennas," *IEEE Trans. Antennas Propag.*, vol. 60, no. 2, pp. 743–750, Feb. 2012.

[24] K. Konstantinidis, A. P. Feresidis, and P. S. Hall, "Multilayer partially reflective surfaces for broadband Fabry–Pérot cavity antennas," *IEEE Trans. Antennas Propag.*, vol. 62, no. 7, pp. 3474–3481, Jul. 2014.

[25] P.-Y. Qin, L.-Y. Ji, S.-L. Chen, and Y. J. Guo, "Dual-polarized wideband Fabry–Pérot antenna with quad-layer partially reflective surface," *IEEE Antennas Wireless Propag. Lett.*, vol. 17, no. 4, pp. 551–554, Apr. 2018.

[26] R. M. Hashmi and K. P. Esselle, "A class of extremely wideband resonant cavity antennas with large directivity-bandwidth products," *IEEE Trans. Antennas Propag.*, vol. 64, no. 2, pp. 830–835, Feb. 2016.

[27] A. Lalbakhsh, M. U. Afzal, K. P. Esselle, and S. L. Smith, "A high-gain wideband EBG resonator antenna for 60 GHz unlicenced frequency band," in *Proc. 12th Eur. Conf. Antennas Propag. (EuCAP)*, London, U.K., Apr. 2018, pp. 1–3.

[28] R. M. Hashmi, B. A. Zeb, and K. P. Esselle, "Wideband high-gain EBG resonator antennas with small footprints and all-dielectric superstructures," *IEEE Trans. Antennas Propag.*, vol. 62, no. 6, pp. 2970–2977, Jun. 2014.

[29] A. A. Baba, R. M. Hashmi, and K. P. Esselle, "Achieving a large gain-bandwidth product from a compact antenna," *IEEE Trans. Antennas Propag.*, vol. 65, no. 7, pp. 3437–3446, Jul. 2017.

[30] A. A. Baba, R. M. Hashmi, K. P. Esselle, and A. R. Weily, "Compact high-gain antenna with simple all-dielectric partially reflecting surface," *IEEE Trans. Antennas Propag.*, vol. 66, no. 8, pp. 4343–4348, Aug. 2018.

[31] N. Nguyen-Trong, H. H. Tran, T. K. Nguyen, and A. M. Abbosh, "Wideband Fabry–Pérot antennas employing multilayer of closely spaced thin dielectric slabs," *IEEE Antennas Wireless Propag. Lett.*, vol. 17, no. 7, pp. 1354–1358, Jul. 2018.

[32] A. Lalbakhsh, M. U. Afzal, K. P. Esselle, and S. L. Smith, "Wideband near-field correction of a Fabry–Pérot resonator antenna," *IEEE Trans. Antennas Propag.*, vol. 67, no. 3, pp. 1975–1980, Mar. 2019.

[33] A. Lalbakhsh, M. U. Afzal, K. P. Esselle, and S. L. Smith, "Low-cost nonuniform metallic lattice for rectifying aperture near-field of electromagnetic bandgap resonator antennas," *IEEE Trans. Antennas Propag.*, vol. 68, no. 5, pp. 3328–3335, May 2020.

[34] M. U. Afzal, L. Matekovits, K. P. Esselle, and A. Lalbakhsh, "Beam-scanning antenna based on near-electric field phase transformation and refraction of electromagnetic wave through dielectric structures," *IEEE Access*, vol. 8, pp. 199242–199253, 2020.

[35] Y. Zheng *et al.*, "Wideband gain enhancement and RCS reduction of Fabry–Pérot resonator antenna with chessboard arranged metamaterial superstrate," *IEEE Trans. Antennas Propag.*, vol. 66, no. 2, pp. 590–599, Feb. 2018.

[36] A. Lalbakhsh, M. U. Afzal, K. P. Esselle, S. L. Smith, and B. A. Zeb, "Single-dielectric wideband partially reflecting surface with variable reflection components for realization of a compact high-gain resonant cavity antenna," *IEEE Trans. Antennas Propag.*, vol. 67, no. 3, pp. 1916–1921, Mar. 2019.

[37] Z. Liu, S. Liu, X. Zhao, X. Kong, Z. Huang, and B. Bian, "Wideband gain enhancement and RCS reduction of Fabry–Pérot antenna using hybrid reflection method," *IEEE Trans. Antennas Propag.*, vol. 68, no. 9, pp. 6497–6505, Sep. 2020.

[38] Z. Liu *et al.*, "A low-RCS, high-GBP Fabry–Pérot antenna with embedded chessboard polarization conversion metasurface," *IEEE Access*, vol. 8, pp. 80183–80194, 2020.

[39] Y. Cheng and Y. Dong, "Bandwidth enhanced circularly polarized Fabry–Pérot cavity antenna using metal strips," *IEEE Access*, vol. 8, pp. 60189–60198, 2020.

[40] Q.-Y. Guo and H. Wong, "Wideband and high-gain Fabry–Pérot cavity antenna with switched beams for millimeter-wave applications," *IEEE Trans. Antennas Propag.*, vol. 67, no. 7, pp. 4339–4347, Jul. 2019.

[41] L.-Y. Ji, P.-Y. Qin, and Y. J. Guo, "Wideband Fabry–Pérot cavity antenna with a shaped ground plane," *IEEE Access*, vol. 6, pp. 2291–2297, 2018.

[42] A. Lalbakhsh, M. U. Afzal, and K. P. Esselle, "Multiobjective particle swarm optimization to design a time-delay equalizer metasurface for an electromagnetic band-gap resonator antenna," *IEEE Antennas Wireless Propag. Lett.*, vol. 16, pp. 912–915, 2017.

[43] L. Zhou, X. Duan, Z. Luo, Y. Zhou, and X. Chen, "High directivity Fabry–Pérot antenna with a nonuniform partially reflective surface and a phase correcting structure," *IEEE Trans. Antennas Propag.*, vol. 68, no. 11, pp. 7601–7606, Nov. 2020.

Zhiming Liu was born in Jiangxi, China, in 1989. He received the B.S. degree from the East China Institute of Technology, Fuzhou, China, in 2012, the M.S. degree from Nanchang University, Nanchang, China, in 2015, and the Ph.D. degree from the College of Electronic and Information Engineering, Nanjing University of Aeronautics and Astronautics, Nanjing, China, in 2019.

From 2019 to 2020, he was a Post-Doctoral Research Fellow with the Department of Electrical and Computer Engineering, University of Victoria, Victoria, BC, Canada. He is now with the School of Information Engineering, Nanchang University. His current research interests include antennas and metasurfaces.

Jens Bornemann (Life Fellow, IEEE) received the Dipl.-Ing. and Dr.-Ing. degrees in electrical engineering from the University of Bremen, Bremen, Germany, in 1980 and 1984, respectively.

From 1984 to 1985, he worked as an Engineering Consultant. In 1985, he joined the University of Bremen, as an Assistant Professor. Since April 1988, he has been with the Department of Electrical and Computer Engineering, University of Victoria, Victoria, BC, Canada, where he became a Professor in 1992. From 1992 to 1995, he was a fellow of the British Columbia Advanced Systems Institute. In 1996, he was a Visiting Scientist at Spar Aerospace Ltd. (now MDA Space), Sainte-Anne-de-Bellevue, QC, Canada, and a Visiting Professor at the Microwave Department, University of Ulm, Ulm, Germany. From 1997 to 2002, he was the Co-Director of the Center for Advanced Materials and Related Technology (CAMTEC), University of Victoria. He served as an Associate Editor for the IEEE TRANSACTIONS ON MICROWAVE THEORY AND TECHNIQUES in the area of microwave modeling and CAD from 1999 to 2002. From 2006 to 2008, he was an Associate Editor of the *International Journal of Electronics and Communications*. In 2003, he was a Visiting Professor at the Laboratory for Electromagnetic Fields and Microwave Electronics, ETH Zürich, Zürich, Switzerland. He has coauthored *Waveguide Components for Antenna Feed Systems: Theory and Design* (Artech House, 1993) and has authored or coauthored more than 350 technical papers. His research activities include RF/wireless/microwave/millimeter-wave components and systems design, and field-theory-based modeling of integrated circuits, feed networks, and antennas.

Dr. Bornemann is a fellow of the Canadian Academy of Engineering (CAE) and the Engineering Institute of Canada (EIC). He is a Registered Professional Engineer in the Province of British Columbia, Canada. He serves on the Editorial Advisory Board of the *International Journal of Numerical Modelling*. From 1999 to 2009, he served on the Technical Program Committee of the IEEE MTT-S International Microwave Symposium.

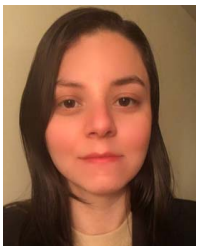

Deisy Formiga Mamedes (Graduate Student Member, IEEE) received the B.S. and M.Sc. degrees in electric engineering from the Federal Institute of Paraiba, João Pessoa, Brazil, in 2016 and 2018, respectively. She is currently pursuing the Ph.D. degree in electrical engineering with the University of Victoria, Victoria, BC, Canada.

She worked as an Instructor from 2017 to 2018 at the Federal Institute of Rio Grande do Norte, Mossoró, Brazil, and from 2018 to 2019 at the Senai College of Paraiba, João Pessoa. She has authored or coauthored over 30 technical papers. Her research interests include microwave and millimeter-wave components, modeling of integrated circuits, and frequency selective surface and antennas.

Shaobin Liu (Member, IEEE) received the Ph.D. degree in electronics science and technology from the National University of Defense Technology, Changsha, China, in 2004.

However, in 2003, he was already promoted as a Professor. He is currently a Professor of electromagnetic and microwave technology at the Nanjing University of Aeronautics and Astronautics, Nanjing, China. His research focuses on plasma stealthy antennas, microwave, radio frequency, and electromagnetic compatibility.

Xiangkun Kong (Member, IEEE) received the Ph.D. degree in communication and information systems from the Nanjing University of Aeronautics and Astronautics (NUAA), Nanjing, China, in 2015.

He has been an Associate Professor with NUAA since his promotion in July 2015. He used to work at the University of St. Andrews, St. Andrews, U.K., as an Academic Visitor supported by the China Scholarship Council. He has published more than 100 articles in different academic journals, including *Applied Physics Letters*, *Optics Express*, and the IEEE JOURNAL OF SELECTED TOPICS IN QUANTUM ELECTRONICS, and has been cited 1800 times. His main research interests include the electromagnetic properties of metamaterials, metamaterials and metasurface application, plasma photonic crystal, and computational electromagnetics.

Xing Zhao was born in Tianjin, China. He received the B.Eng. degree in information engineering from Shanghai Jiao Tong University, Shanghai, China, in 2008, and the M.S. and Ph.D. degrees in electronics and computer engineering from Hanyang University, Seoul, South Korea, in 2010 and 2014, respectively.

From 2015 to 2017, he was a Post-Doctoral Research Fellow with the Department of Electrical and Computer Engineering, National University of Singapore, Singapore. He is currently an Associate Research Fellow with the College of Electronic and Information Engineering, Nanjing University of Aeronautics and Astronautics, Nanjing, China. His current research interests include small antennas for 5G mobile MIMO platforms and integrated array antennas for radar systems.